Nanostructure by high-energy X-ray diffraction

Detailed knowledge of the atomic-scale structure is needed to understand and predict properties of materials. For ordinary crystals, this information is obtained by traditional (Bragg) X-ray diffraction. It is difficult to use this approach on materials structured at the nanoscale because their diffraction patterns show few, if any, Bragg peaks, and have a pronounced diffuse component. A non traditional approach based on high-energy X-ray diffraction and atomic pair distribution function data analysis may be used instead. This article describes the essentials of this approach and its great potential. The purpose is to encourage the nanoscience community go beyond traditional X-ray diffraction.

Valeri Petkov*

Department of Physics, Central Michigan University, Mt Pleasant, MI 48859, USA

**Email: petkov@phy.cmich.edu – url: http://www.phy.cmich.edu/people/petkov*

X-Ray Diffraction (XRD) has long been used to determine the atomic-scale structure of materials. This technique is based on the fact that the wavelength of X-rays is comparable to the distances between atoms in condensed matter. When a material exhibiting a long-range (i.e. at least micrometers), periodic atomic order, such as a crystal, is irradiated with X-rays it acts as an extended, well-defined grating and produces a diffraction pattern showing numerous sharp spots, called Bragg diffraction peaks. By measuring and analyzing the positions and intensities of these peaks it is possible to determine the spatial characteristics of the grating – i.e. to determine the three-dimensional (3-D) arrangement of atoms in the crystalline material being studied.

This is the essence of 'crystal structure' determination by XRD[1]. Over the years the technique has been refined and applied successfully to a variety of crystalline materials – from simple solids to complex proteins. XRD has also been successfully applied to study the structure of materials where atoms are ordered only at short distances (i.e. less than a nanometer), such as glasses and liquids. When irradiated with X-rays these materials act as very imperfect gratings and produce XRD patterns that are highly diffuse. A specialized approach, known as the atomic Pair Distribution Function (PDF) technique, has been used to analyze diffuse (i.e. non-Bragg type) XRD patterns and obtain important structural information such as nearest neighbor atomic distances and coordination numbers for noncrystalline materials[2]. Thus XRD has proven to be a valuable research tool for both regular crystals and noncrystals. With current technology moving rapidly towards smaller scales, nanocrystalline materials are being produced in increasing numbers. As their name

ISSN:1369 7021 © Elsevier Ltd 2008

implies, nanocrystalline materials show a length of structural coherence from one to several tens of nanometers, i.e. from a structural point of view they fall somewhere between regular crystals and noncrystals. The limited degree of structural coherence in a nanocrystalline material may be due to one of the following reasons: (i) the material may show a very well-defined atomic ordering but its physical size is in the nanometer range, e.g. nanotubes; (ii) the physical size of the material may be quite large (e.g. micrometers) but atoms inside it are ordered over distances of only a few nanometers, e.g. sintered nanoceramics. In either case a nanocrystalline material would to a certain extent act as a grating, and hence produce XRD patterns showing both Bragg-like peaks and a diffuse component (see the various examples discussed below). These Bragg-like peaks are, however, neither as sharp nor as numerous as those observed in the XRD patterns of regular crystals. In addition, the diffuse component is very strong, similar to what is observed with noncrystals, and cannot be neglected. This renders traditional (Bragg) X-ray crystallography of these materials very difficult, if not impossible[3]. However, a combination of high-energy XRD and atomic PDF data analysis can be used to successfully tackle the problem.

Atomic PDF essentials

The frequently used reduced atomic PDF, $G(r)$, gives the number of atoms in a spherical shell of unit thickness at a distance r from a reference atom as follows:

$$G(r) = 4\pi r[\rho(r) - \rho_o], \tag{1}$$

where $\rho(r)$ and ρ_o are the local and average atomic number densities, respectively, and r is the radial distance. As defined, $G(r)$ is a one-dimensional function that oscillates around zero and shows positive peaks at distances separating pairs of atoms, i.e. where the local atomic density exceeds the average. The negative valleys in $G(r)$ correspond to real space vectors lacking atoms at either of their ends. In this respect $G(r)$ resembles the so-called Patterson function that is widely applied in traditional X-ray crystallography[1]. However, while the Patterson function is discrete and peaks at interatomic distances within the unit cell of a crystal, $G(r)$ is a continuous function reflecting all interatomic distances occurring in a material. This is a great advantage when studying materials whose structure is difficult to describe in terms of extended periodic lattices. $G(r)$ is the Fourier transform of the experimentally observable total structure function, $S(Q)$, i.e.

$$G(r) = (2/\pi)\int_{Q=o}^{Q_{max}} Q[S(Q)-1]\sin(Qr)dQ, \tag{2}$$

where Q is the magnitude of the wave vector ($Q = 4\pi\sin\theta/\lambda$), 2θ is the angle between the incoming and outgoing X-rays, and λ is the wavelength of the X-rays used[2]. XRD usually employs the so-called Faber–Ziman-type structure function, $S(Q)$, which is related to the coherent part of the diffraction pattern, $I^{coh.}(Q)$, as follows[4]:

$$S(Q) = 1 + \left[I^{coh.}(Q) - \sum c_i \left|f_i\ (Q)\right|^2\right] / \left|\sum c_i f_i(Q)\right|^2, \tag{3}$$

where c_i and $f_i(Q)$ are the atomic concentration and X-ray scattering factor, respectively, for the atomic species of type i. It should be noted that for a material comprising n atomic species, a single diffraction experiment yields a total atomic distribution function, $G(r)$, which is a weighted sum of $n(n + 1)/2$ partial PDFs, $G(r_{ij})$, i.e.

$$G(r) = \sum_{i,j} w_{ij} G_{ij}(r)\ . \tag{4}$$

Here w_{ij} are weighting factors depending on the concentration and scattering power of the atomic species as follows:

$$w_{ij} = c_i c_j f_i(Q) f_j(Q) / \sum [c_i f_i(Q)]^2\ . \tag{5}$$

For practical purposes w_{ij}s are often evaluated[2,4] for $Q = 0$. As can be seen from Eqs. (1)–(5), the atomic PDF is simply another representation of the experimental XRD data. However, exploring the XRD data in real space is advantageous, especially when studying nanocrystalline materials. Firstly, as Eq. (3) implies, the *total* scattering, including Bragg-like peaks as well as diffuse (non-Bragg-like) scattering, contributes to the PDF. In this way both the discernible atomic order, manifested in the Bragg-like peaks, and all structural 'imperfections' that are responsible for its limited extent, manifested in the intense diffuse component of the diffraction pattern, are reflected in the experimental PDF for a nanocrystalline material. Secondly, by accessing high values of Q, experimental PDFs of improved real-space resolution[5] can be obtained, and hence all the important details in the atomic-scale structure of a nanocrystal are revealed. Thirdly, the atomic PDF is hardly influenced by diffraction optics and experimental factors since these are accounted for in the step of extracting the coherent intensities from the raw XRD data (see Eq. (3)). This makes the PDF an experimental quantity that directly yields relative positions of atoms, enabling a convenient testing and refinement of 3-D structural models, as demonstrated by the examples shown below.

High-energy XRD experimental procedures

Source of radiation

Diffraction data at higher wave vectors (~20 Å^{-1} and higher) can be obtained using X-rays of shorter wavelengths, i.e. of higher energy. Such X-rays may be obtained from synchrotron or laboratory sources (e.g. sealed X-ray tubes with a Mo (energy ~17 keV) or Ag (energy ~22 keV) anode). For reference, the energy of Cu K_α radiation is only about 8 keV, and hence this is not suitable for high-energy XRD.

Data statistics and collection time

Whatever the source of high-energy X-rays, the diffraction data should be collected with a very good statistical accuracy – much better (let us say an order of magnitude better) than that required for traditional (e.g. Rietveld) analysis. To achieve this accuracy, longer than usual XRD data collection times should be used[6,7]. This may amount to many tens of hours if a sealed X-ray tube source and a single point (e.g. scintillation) detector are employed. Synchrotron X-rays and large-area detectors can reduce the data collection times to seconds[8].

Spatial resolution of the experimental set-up

In general, structural studies on nanocrystalline materials do not require experimental set-ups with very high reciprocal space resolution because of the inherently diffuse nature of the XRD patterns that are to be collected. However, care should be taken that the reciprocal space resolution of the experimental set-up, including the detector, is not too low[9]. As an example, XRD patterns for Si (NIST powder standard) collected with two different types of detectors, a single-point, solid-state detector and a mar345 Image Plate Detector, are shown in Fig. 1. The lower resolution of the XRD data collected with the Image Plate Detector leads to an extra broadening of the peaks

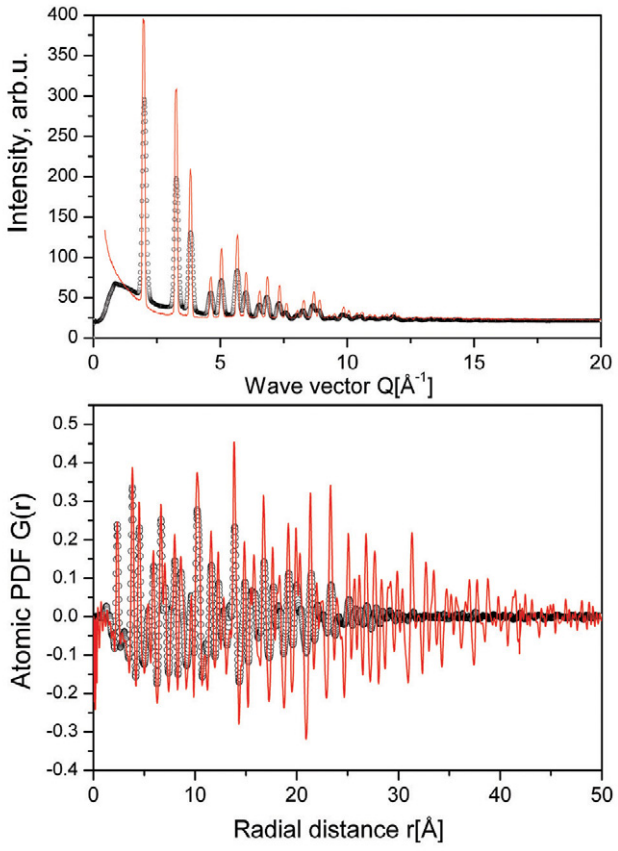

Fig. 1 Experimental XRD patterns for Si standard collected with a point detector (solid red line) and a mar345 Image Plate Detector (symbols) while the rest of the experimental set-up was kept unchanged. The corresponding atomic PDFs are shown in the lower part of the plot.

in the XRD pattern, and hence to a loss of information in the higher-*r* region of the corresponding atomic PDF. This loss may be critical or not depending on the complexity of the atomic ordering in the nanocrystalline material studied.

Background signal treatment

Scattering from air, the sample holder, the background, etc., should be kept to a minimum since atomic PDFs are based on only the elastic component of XRD patterns converted to absolute (i.e. electron) units (see Eq. (3)). As practice has repeatedly shown, it is always easier to correct for a weak background signal than for a strong one.

Sample related 'unwanted' signal

X-rays are both scattered from and absorbed inside materials via various processes. The attenuation of high-energy X-rays is relatively low and usually does not pose much of a problem in structural studies of nanocrystalline materials. The same is true for multiple scattering of high-energy X-rays. Inelastic (Compton) scattering, however, may be very strong, especially at high wave vectors, and should be very carefully eliminated from the raw XRD data either by using energy-sensitive detectors[10] or analytically. Fluorescent scattering from the sample may be reduced by using, when possible, X-rays with an energy below the absorption edge of the most strongly scattering atomic species in the material under study. The combined effect of all these factors on the various experimental geometries has been fully discussed in the literature[11].

High-energy XRD aimed at atomic PDF data analysis thus may appear somewhat involved, but in reality it is not very much different from traditional powder XRD provided the experiment is carried out with due care, as described above. As an example, high-energy XRD patterns for bulk (i.e. polycrystalline) and 5 nm particles of CdTe are shown in Fig. 2. The data were collected at the beamline 11-ID-C (Advanced Photon Source, Argonne National Laboratory) using synchrotron radiation of energy 115.227 keV (λ = 0.1076 Å) and a large area (mar345) detector. Data collection times were of the order of half an hour per sample. As can be seen in Fig. 2, the XRD pattern for polycrystalline CdTe shows many sharp Bragg peaks as expected for a material possessing long-range, periodic atomic order. The XRD pattern for nanocrystalline CdTe shows only a few very broad Bragg-like peaks at low wave vectors (<5 Å^{-1}). The much more diffuse nature and greatly diminished number of well-resolved peaks is indeed what renders the XRD patterns of nanocrystalline materials very difficult to analyze in the traditional (e.g. Rietveld[12]) way.

Structure factors extracted from the two XRD data sets (see the lower part of Fig. 2), however, exhibit physical (i.e. not noise-based) oscillations, which reach a maximum value of 30 Å^{-1} in this experiment. The higher-frequency oscillations in the structure factors come from the Bragg-like peaks in the XRD data, and reflect the longer-range atomic order. The low-frequency ones come from the diffuse-like

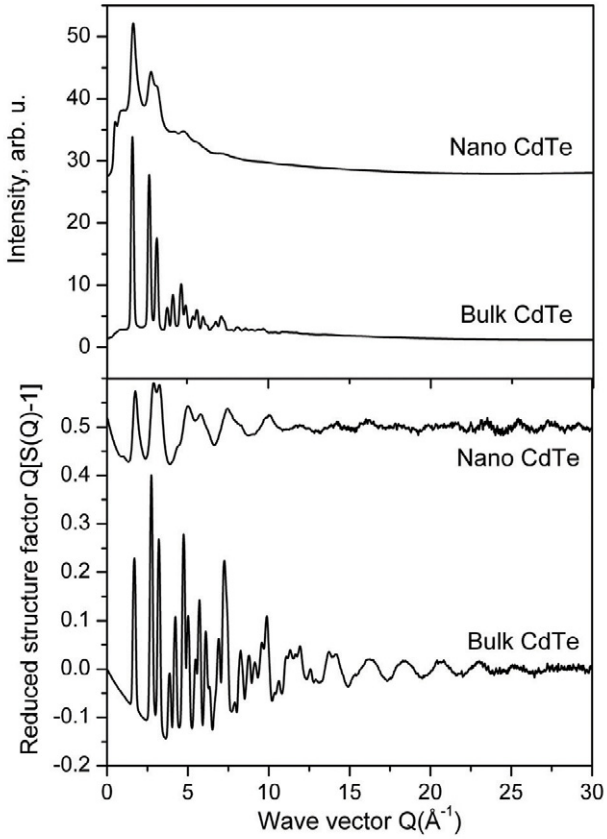

Fig. 2 Synchrotron XRD patterns (upper part) and the corresponding structure factors (lower part) for polycrystalline and nanocrystalline CdTe.

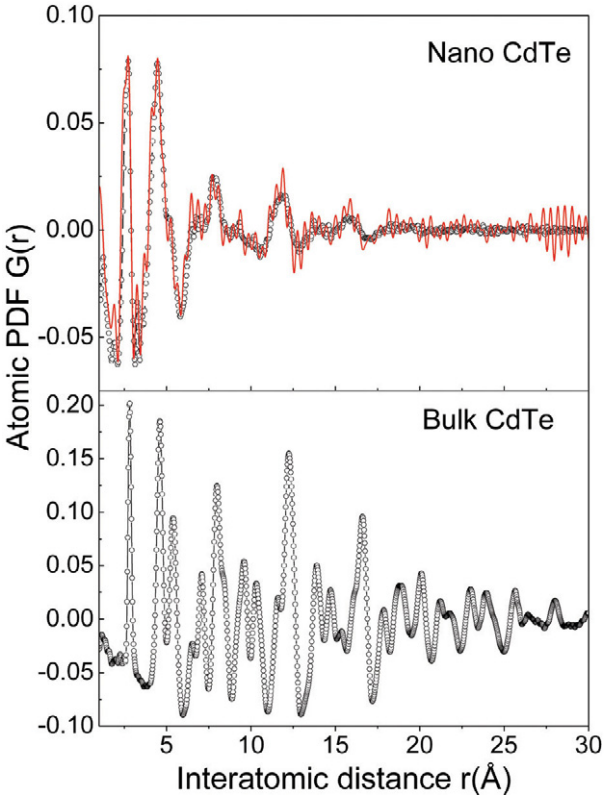

Fig. 3 Experimental (black symbols) PDFs for bulk and 5 nm CdTe based on the synchrotron XRD data shown in Fig. 1. An experimental PDF obtained with the use of in-house equipment (Mo Kα) radiation is also shown (red line).

component in the XRD data, and reflect the structural imperfections that limit this order. Note that many of those physical oscillations remain 'hidden' in the raw XRD patterns but are clearly revealed in the corresponding $Q[S(Q) - 1]$ plots thanks to the rigorous data corrections and normalization done in the course of PDF data analysis. This is indeed one of the major differences between the traditional XRD and the nontraditional approach described here. The former relies only on sharp and intense Bragg peaks appearing at relatively low-Q values (usually less than 10 Å^{-1}; see Fig. 1), and hence is mostly sensitive to long-range, periodic atomic ordering in materials. Total XRD/PDF uses all physical oscillations (information!) stored in the diffraction data up the highest wave vector reached, and hence is sensitive to atomic ordering of any extent and periodicity. This is clearly demonstrated by the experimental data shown in Fig. 3. The experimental PDF for polycrystalline CdTe is seen to show distinctive structural features to high interatomic vectors, while that for 5 nm CdTe particles decays to zero much faster, reflecting the substantially reduced length of structural coherence in the latter material. Although decaying fast, the experimental PDF for nanocrystalline CdTe reveals unambiguously the type and symmetry of atomic ordering as well as the presence of strain and a subnanoparticle (core–shell) structure in the material[13]. An experimental PDF for 5 nm CdTe particles based on XRD data obtained on an in-house instrument is also shown in Fig. 3. The data were collected using Mo K_α radiation (resulting in a Q_{max} of 16 Å^{-1}) and a single-point (scintillation) detector for a period of 72 h. This PDF appears somewhat noisy due to insufficient XRD data statistics and the relatively low Q_{max} reached with the particular experimental set-up. However, it still reflects well the basic features of atomic ordering in 5 nm CdTe particles.

In-house equipment optimized for high-energy XRD (e.g. a rotating anode generator, appropriate collimation, and a fast detector sensitive to Mo/Ag K_α radiation) could yield atomic PDFs of quality comparable to that achieved with synchrotron X-ray data. Such an investment may be worthwhile in an industrial or large research institution setting where a large number of nanocrystalline materials are screened on a regular basis, and/or when going to a synchrotron facility is not an option.

High-energy XRD data processing and PDF analysis

Correcting the experimental XRD data (e.g. Fig. 2, upper part) for instrumental effects and converting them to structure factors (e.g. Fig. 2, lower part), and then computing the corresponding atomic PDFs (e.g. Fig. 3) may be done using free software such as RAD[14] or

PDFGetX2[15]. The software is documented, and test examples are also provided. Once good-quality experimental PDFs are obtained, one may proceed with structure search and refinement in a way similar to the traditional Rietveld analysis of XRD patterns. Crystallography-constrained (i.e. described in terms of periodic lattices and 230 space groups) models up to a few hundred atoms may be conveniently tested and refined using the computer code PDFfit2[16]. The computer code DISCUS[17] can be employed to generate structurally disordered yet crystallography-constrained models of a much larger size (many thousands of atoms). A new development in DISCUS are 'evolutionary' refinement algorithms[18], which allow both the structure and morphology of a nanomaterial to be assessed[19]. When the atomic ordering in the 'nanocrystalline' material turns out not to be periodic, reverse Monte Carlo type simulations[20] can do a very good job. Ab initio structure determination[21] may be attempted as well. There is no general recipe as to which type of structure models – crystallographic, heavily disordered yet crystallographic or noncrystallographic (i.e. nonperiodic) – to explore first. Any extra information, such as a material's density, morphology/shape, TEM images, local structure from EXAFS or Raman, etc., may be used to facilitate the structure determination process. The goal should be to obtain a 3-D atomic configuration/model that is simple, i.e. with the smallest possible number of free parameters, yet representative enough to serve as a good structural basis for understanding and predicting all the important properties of the nanocrystalline material under study. The examples shown below illustrate how this is done in practice.

Examples of structural studies of nanocrystalline materials

'Bulk' nanocrystalline materials†

An example of a material that is 'bulk', i.e. with a physical size approaching a micrometer but showing a structural coherence limited to just a few nanometers, is ball-milled zirconia. Zirconia's unique combination of mechanical and electrical properties makes it very useful in applications such as heat insulators, oxygen sensors, fuel cells, and catalyst supports[22]. At atmospheric pressure, pure ZrO_2 is known to adopt three different crystal structures. At high temperature (>2640 K) it has a cubic structure (space group $Fm\bar{3}m$). Between 1440 and 2640 K zirconia is tetragonal ($P4_2/nmc$) and below 1440 K it is monoclinic ($P2_1/c$). The tetragonal to monoclinic phase transition is accompanied by a 3–5% volume increase that causes cracking of bulk zirconia, and hence deteriorates its mechanical properties. This renders pure zirconia virtually useless for technological applications. To remedy the problem, the high-temperature phases (tetragonal or cubic) of zirconia are stabilized at room temperature by reducing the crystallite size by ball milling. The technique has gained particular popularity due to its ease of use and ability to produce large quantities at low cost. Although traditional techniques for structural determination have shown that the high-temperature phases (either tetragonal or cubic) are stabilized in nanocrystalline zirconia prepared by ball milling, some controversy about the type of atomic structure and phase content has arisen. For example, some researchers have observed the formation of tetragonal and amorphous phases in nanocrystalline zirconia obtained by ball milling, while others reported a mixture of monoclinic and cubic phases. To resolve the controversy a structural study using high-energy XRD and atomic PDFs was undertaken. Nanocrystalline zirconia was obtained by ball-milling crystalline ZrO_2 with monoclinic symmetry. Milling for 12 h reduced the polycrystals (with a size of several microns) from the starting material to fine grains of about 300 nm. XRD patterns for the starting material and the products obtained by milling it for different periods of time are shown in Fig. 4.

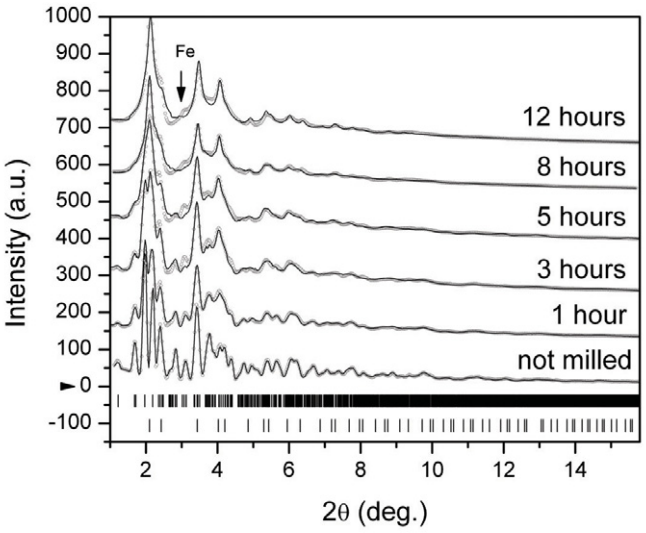

Fig. 4 Experimental synchrotron (114.496 keV; λ = 0.1083 Å) XRD patterns (symbols) for ZrO_2 samples milled for different times and calculated patterns (lines) obtained through a two-phase Rietveld refinement. The positions of the Bragg peaks of the monoclinic (the upper set of bars) and cubic (the lower set of bars) phases are given in the lower part of the plot.

As can be seen in Fig. 4, the XRD pattern of monoclinic (not milled) zirconia exhibits well-defined Bragg peaks up to Q ~ 8–10 $Å^{-1}$. The material is obviously a perfect polycrystalline solid. The Bragg peaks in the XRD patterns of the milled samples are rather broad and merge into a slowly oscillating diffuse component already at Q values as low as 4–5 $Å^{-1}$. Experimental atomic PDFs extracted from the XRD patterns are shown in Fig. 5.

As can be seen in Fig. 5, the experimental PDF for polycrystalline ZrO_2 is rich in well-defined structural features extending to high real-space distances. The PDFs for the ball-milled samples are also rich in well-defined features but these vanish already at 2-3 nm. Obviously, although the ball-milled material is still a 'bulk' phase (a phase composed of grains about 300 nm in size) it has an atomic arrangement that is very well defined at nanoscale (2–3 nm) distances

† *Materials that are bulk (i.e. micrometers or larger in size) and ordered over long-range distances but show nanoscale structural distortions/inhomogeneities (e.g. colossal magnetoresistance materials, thermoelectric clathrates, some multiferroics, high Tc materials etc.) are not considered to be nanocrystalline within the context of this review.*

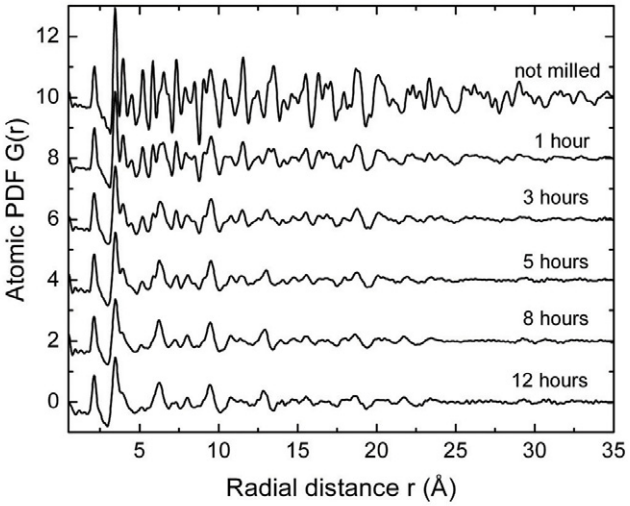

Fig. 5 Atomic PDFs obtained from the powder diffraction patterns of Fig. 4.

only, and, in this sense, is nanocrystalline. To reveal the 3-D atomic ordering in nanocrystalline zirconia, several crystallographic-type structural models were tested by fitting them to the experimental PDF data. The test showed that, on average, nanocrystalline zirconia possesses a structure that may be described in terms of the CaF_2-type atomic ordering which has an orthogonal unit cell. The local atomic ordering (at distances shorter than 5 Å, i.e. within the orthogonal unit cell), however, deviates from the average and resembles that occurring in monoclinic ZrO_2[22].

Other examples of successful high-energy XRD and atomic PDF studies on 'bulk' nanocrystalline materials include structure determinations of ball-milled $MgFe_2O_4$ ferrites[23], restacked WS_2[24], Li-intercalated MoS_2[25], alkali metal manganese oxides used in batteries[26], titania[27], $PbZr_{1-x}TiO_3$[28], $BaTiO_3$ nanoceramics[29], hydrous ruthenia[30], and finely powdered iron phosphate[31].

Free-standing nanosized particles

Nanosized particles have shown very good potential for optical, magnetic, catalytic, and life-science applications (e.g. biolabeling), and hence have been the subject of extensive recent studies. A typical example are Au nanoparticles. While bulk Au is exceptionally inert, Au nanoparticles are optically and catalytically very active. It is widely believed that the improved performance of nanoparticles is due to their greatly enhanced surface-to-volume ratio. Evidence is mounting, however, that the periodicity of the atomic ordering inside nanoparticles may also be an important factor. Experimental synchrotron (X-rays of energy 90.48 keV; 8 = 0.137 Å) XRD patterns for polycrystalline (bulk) Au and 1.6 nm Au particles (both dissolved in water and dried out) are shown in Fig. 6a. The particles were grown inside the cavities of a seventh-generation polyaminoamide (PAMAM) dendrimer[32]. Sharp Bragg peaks are present in the XRD pattern for polycrystalline Au. The XRD patterns for 1.6 nm Au particles are very diffuse, as is often observed with materials whose structure lacks an

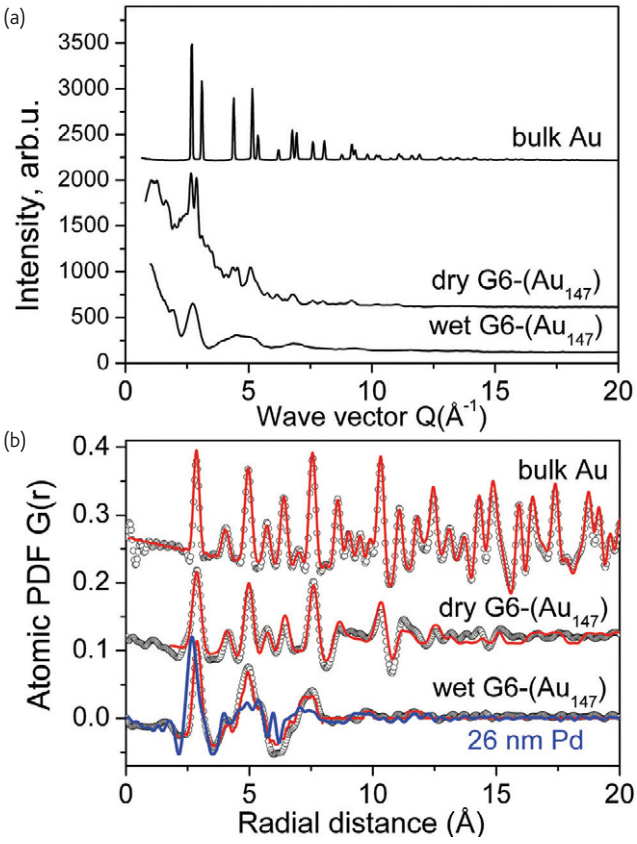

Fig. 6 Experimental XRD (a) and the corresponding PDF G(r) for 1.6 nm Au particles (b) and bulk Au. Best model PDFs (red line) and an experimental PDF for 26 nm Pd particles (blue line) are also shown.

extended atomic order. The corresponding atomic PDFs are shown in Fig. 6b.

The PDF *G*(*r*) for bulk Au exhibits a series of well-defined peaks to high real-space distances each reflecting a particular, well-defined coordination sphere. The experimental data can be approximated very well in terms of a structure based on a periodic (face-centered cubic (fcc)) type lattice (space group *Fm-3m*) with a four-atom unit cell, 4.07 Å in length. The first peak in the experimental PDFs for the nanoparticles is positioned at 2.87(2) Å, consistent with the first-neighbor distance in bulk Au, confirming the metallic character (i.e. the zero valence state) of nanosized (1.6 nm) gold. However, the peaks in the PDFs for Au particles are very broad and decay to zero at distances as short as 10–15 Å. Clearly the sequence of coordination spheres in the nanoparticles is neither as well defined nor so extended as it would be in a nanosized stack of well-defined atomic planes of an fcc lattice. The observed structural disorder may not be neglected, because it rendered unsuccessful all attempts to approximate the experimental PDF data for Au particles with models based on periodic structures. Nonperiodic structure-type models generated by reverse Monte Carlo simulations did a much better job. Exemplary structure models for wet (i.e. in water) and dry 1.6 nm Au particles are shown in Fig. 7.

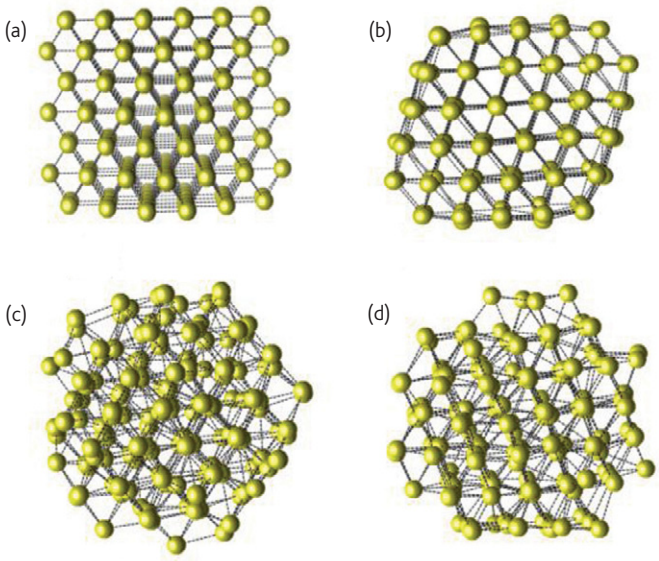

Fig. 7 Fragment (147-atom) of the fcc lattice of bulk Au (a), 140-atom truncated octahedron as generated by DFT alone (b), and RMC-generated models of wet (c) and dry (d) 1.6 nm Au particles.

A 147-atom fragment of the fcc lattice of bulk Au, and a truncated octahedron of 140 atoms obtained from Density Functional Theory (DFT) model calculations are also shown in Fig. 7.

The result indicates that Au nanoparticles do not appear with a fcc or other periodic, lattice-type structure. Instead they are a nonperiodic, dense packing of Au atoms that shows some characteristics of the fcc-type structure only. Periodicity is a rigid constraint on the structure and properties of bulk regular crystals. Apparently it may be partially or fully broken in nanosized particles of crystals, and hence may be used as an extra (i.e. in addition to the increased surface to volume ratio) parameter to fine-tune their properties[32]. Other examples of successful high-energy XRD and atomic PDF studies on nanosized particles include structural determination of nanosized Ru[33], PdFe[34], GaN[35], and semiconductor quantum devices[36–39]. When needed, extra chemical specificity may be achieved by employing resonant high-energy XRD as demonstrated in a study on supported Au particles[40].

Novel nanostructures

Nanocrystalline materials may also possess an unusual shape/morphology – 'blackberry'[41], 'tetrapod'[42], 'tube'[43], etc. These unusual morphologies endow the materials with novel properties and may often impose an atomic arrangement that is quite different from that found in the corresponding bulk solids. A typical example are V_2O_5 nanotubes. Crystalline V_2O_5 is a key technological material widely used in applications such as optical switches, chemical sensors, catalysts, and solid-state batteries. The material possesses outstanding structural versatility and can be manufactured into nanotubes that significantly enhance many of the useful physicochemical properties of the parent V_2O_5 crystal. For example, the high specific surface area of the

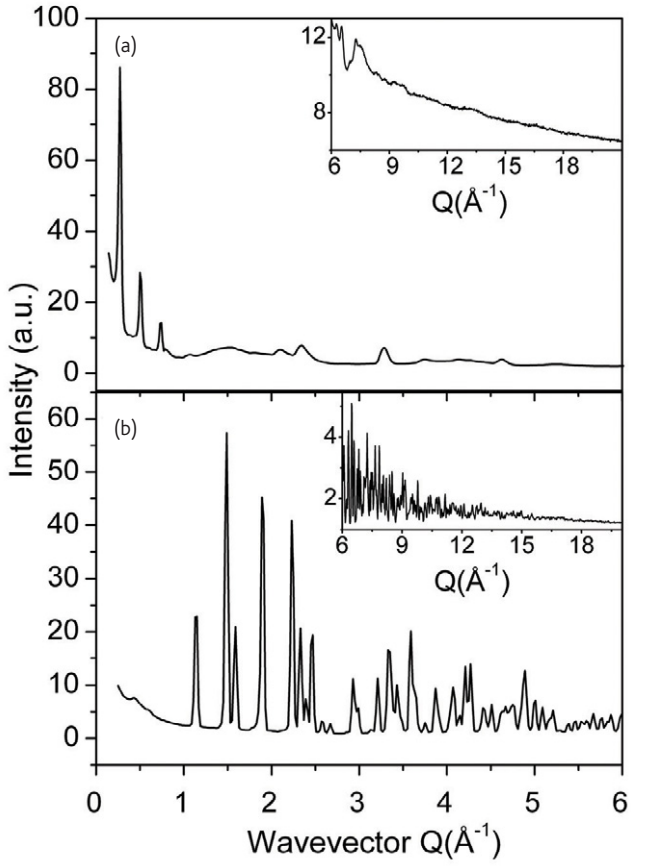

Fig. 8 Experimental synchrotron XRD patterns for V_2O_5 nanotubes (a) and crystalline V_2O_5 (b). The high-Q portion of the patterns is given in the insets on an enlarged scale.

nanotubes renders them even more attractive as positive electrodes in secondary Li batteries. The nanotubes also show significantly increased capability for redox reactions. Furthermore, the nanotubes show good potential for completely novel applications such as nanoactuators and nonlinear optical limiters[43]. High-energy XRD experiments on V_2O_5 nanotubes and polycrystalline V_2O_5, used as a standard, were carried out at the 1-ID beam line at the Advanced Photon Source (APS) using 80.6 keV X-rays. The experimental XRD data are shown in Fig. 8.

As can be seen in Fig. 8 the lack of long-range order due to the curvature of the tube walls has a profound effect on the diffraction pattern of nanocrystalline V_2O_5. While the diffraction pattern of polycrystalline V_2O_5 shows sharp Bragg peaks up to wave vectors as high as $Q \sim 15$ Å^{-1}, that of the nanotube counterpart shows only a few Bragg-like features that merge into a slowly oscillating diffuse component at Q values as low as ~6–8 Å^{-1}. The Bragg-like features in the diffraction pattern of the nanotubes can be subdivided into two groups. The first one includes three relatively sharp peaks seen at wave vectors shorter than 1 Å^{-1} (see Fig. 8a). Those peaks reflect the spacing (≈ 20 Å) between the individual V_2O_5 layers building the walls of the nanotubes and shift whenever a different organic molecule is used

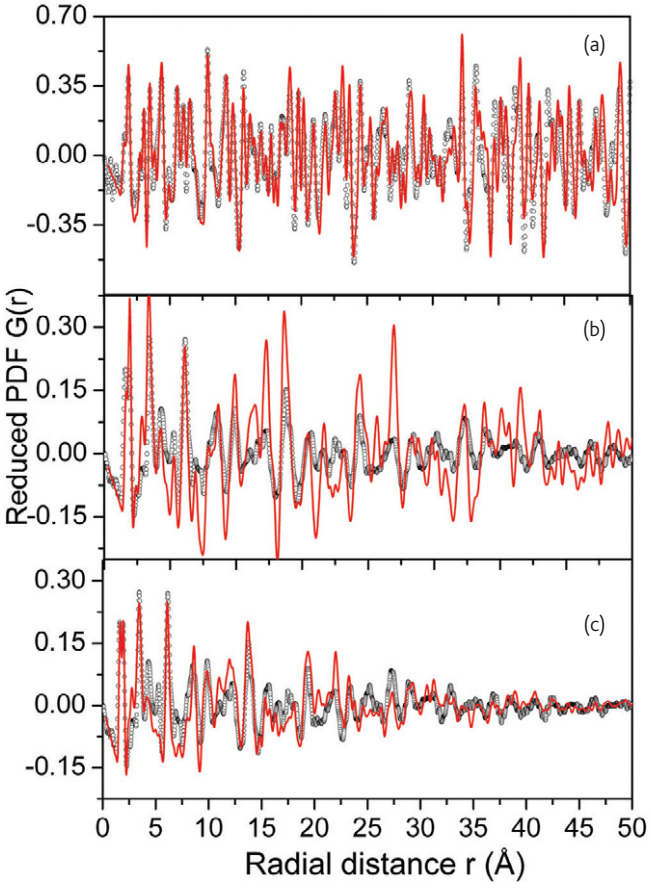

Fig. 9 Comparison between experimental (circles) and model (solid red line) PDFs for: (a) crystalline V_2O_5 and its well-known orthorhombic structure, (b) V_2O_5 nanotubes and the triclinic $BaV_7O_{16}.nH_2O$-type structure, and (c) V_2O_5 nanotubes and a structure model refined against the experimental PDF data[43].

as a nanostructure-directing template. The second group includes all higher-*Q* peaks which, contrary to the lower-*Q* ones, do not change their position as the organic template changes, and may therefore be associated with atomic ordering within the V_2O_5 layers. The finding suggests the presence of well-defined structural units that build the nanotube walls in a repetitive manner. The type of structural units and their coupling scheme was revealed by testing several structural models against the experimental PDF data . A model was found that reproduced the experimental PDF for the nanotubes to an acceptable level, i.e. to the level to which the well-known orthorhombic structure of crystalline V_2O_5 reproduces the respective experimental PDF data (see Fig. 9). A fragment of this structure model and the way it reproduces the nanotube morphology are shown in Fig. 10. This structural study shows that even a nanocrystalline material with the complex morphology of a 'tube' possesses an atomic-scale structure that may be described accurately in terms of a unit cell and symmetry. The unit cell of V_2O_5 nanotubes is of triclinic $P\bar{1}$ symmetry, with dimensions of approximately $6 \times 6 \times 19$ Å, and contains only 46 atoms arranged in a pattern of double layers of $V–O_6$ octahedra (see Fig. 10).

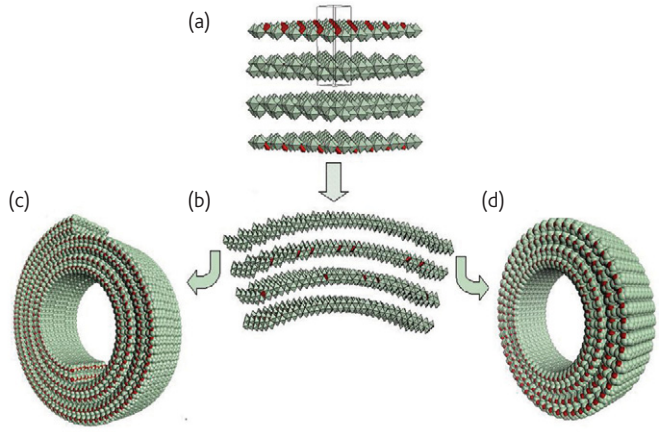

Fig. 10 Structure description of V_2O_5 nanotubes. Double layers of $V–O_6$ octahedral (light green) and $V–O_4$ tetrahedral (red) units are undistorted and stacked in perfect registry with crystalline $BaV_7O_{16}.nH_2O$ (a). When bent (b), such layers may form nanoscrolls (c) or closed nanotubes (d). The real-size models shown in (c) and (d) have an inner diameter of ~10 nm and involve 33,000 atoms.

High-energy XRD and atomic PDF studies have also been successfully applied to determine the 3-D structure of titania nanosheets[44] and nanotubes[45] as well as Mo–S–I nanowires[46].

Organic nanostructures

The primary attraction of organic nanostructures is their low cost and extreme flexibility, which allows devices to be engineered with properties tailored to meet the needs of a particular application. Organic nanostructures are easily integrated with conventional semiconductor devices, thereby providing additional functionality to existing photonic circuits and components. A typical example are dendrimers. Dendrimers are a novel class of organic nanostructure derived via a so-called 'branches-upon-branches' growing process. Branches radiate from a central core and are synthesized through a repetitive reaction sequence that guarantees a complete shell for each generation, leading to polymeric-type macromolecules that are globular in shape and are monodisperse. Seventh-generation PAMAM dendrimers, with an average size of about 9 nm, have been studied using 29.09 keV X-rays (λ=0.425). Hyperbranched PAMAM nanostructures that are easier to produce but do not have the regular structure of dendrimers, as well as fullerene (C_{60}), were also measured[47]. Experimental atomic PDFs extracted from the high-energy XRD data are shown in Fig. 11.

The PDFs all show a strong peak centered at approximately 1.54 Å which is the first neighbor distance within the C backbone of the materials studied. In addition, the first peak in the PDFs for dendritic and hyperbranched nanostructures has a low-*r* pre-peak at 1.1 Å. This is the H–C pair distance in these polymeric materials. Obviously high-energy XRD and atomic PDFs are sensitive to light atomic species, including H, contrary to common belief.

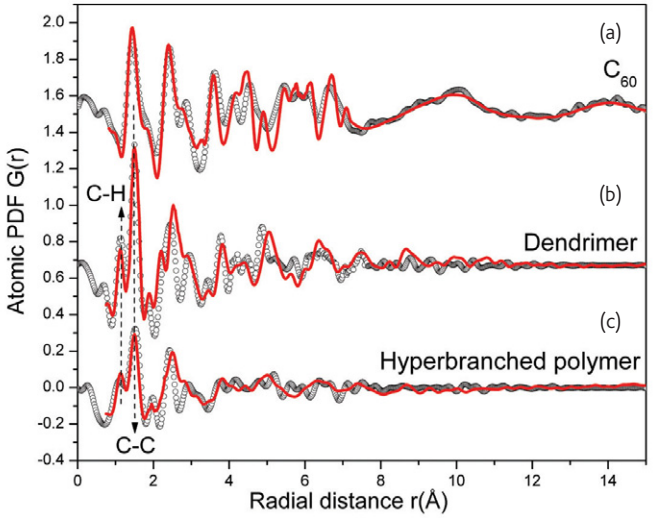

Fig. 11 Experimental (symbols) and model (solid line) atomic PDFs for (a) crystalline C_{60}, (b) dendritic and (c) hyperbranched PAMAM. First PDF peaks are labeled with the corresponding atomic pairs. The model atomic PDFs shown in (a), (b) and (c) are calculated from the atomic configurations presented in Fig. 12a–c, respectively.

Fullerene is a molecular crystal made of rigid units ordered in a fcc arrangement as shown in Fig. 12a. Each fullerene molecule consists of 60 carbon atoms bonded in a nearly spherical configuration enclosing a cavity with a diameter of 7.1 Å. Since the molecule is rigid, all interatomic distances within it are well defined and the corresponding peaks in the atomic PDF are well resolved (see Fig. 11a). At room temperature, C_{60} molecules spin almost freely in their crystal positions, so they look like soccer balls. The correlation between the C atoms from neighboring molecules is lost and, starting at 7.1 Å, the atomic PDF turns into a low-frequency oscillation reflecting the 'ball–ball' correlations. A model PDF calculated from the crystal structure data for fullerene is shown in Fig. 11a. The agreement between the calculated and experimental PDF data is very good. The results for the fullerene demonstrate that atomic PDFs are sensitive to both intra- and intermolecular ordering of organic nanosized materials and may serve as a reliable basis for studying their structural characteristics. If the molecular branches in dendrimers are arranged in a regular pattern and enclose nanosized cavities, just as C_{60} molecules in fullerene do, then the atomic PDF for dendrimers should bear similarities to that of fullerene. A careful inspection of the experimental data presented in Fig. 11b suggests that this indeed may be the case since the PDF for PAMAM dendrimers too shows a series of well-defined peaks extending to ~8 Å followed by an almost featureless tail. Three-dimensional models for the polymeric nanostructures were constructed by *ab initio* calculations followed by molecular dynamics simulations[47]. The models were refined until a good agreement with the experimental PDF data was achieved. The thus-obtained model of a seventh-generation PAMAM dendrimer involving 9186 atoms (C, N, O, and H) is shown in Fig. 12a (left). As can be seen, the model atomic configuration is fairly

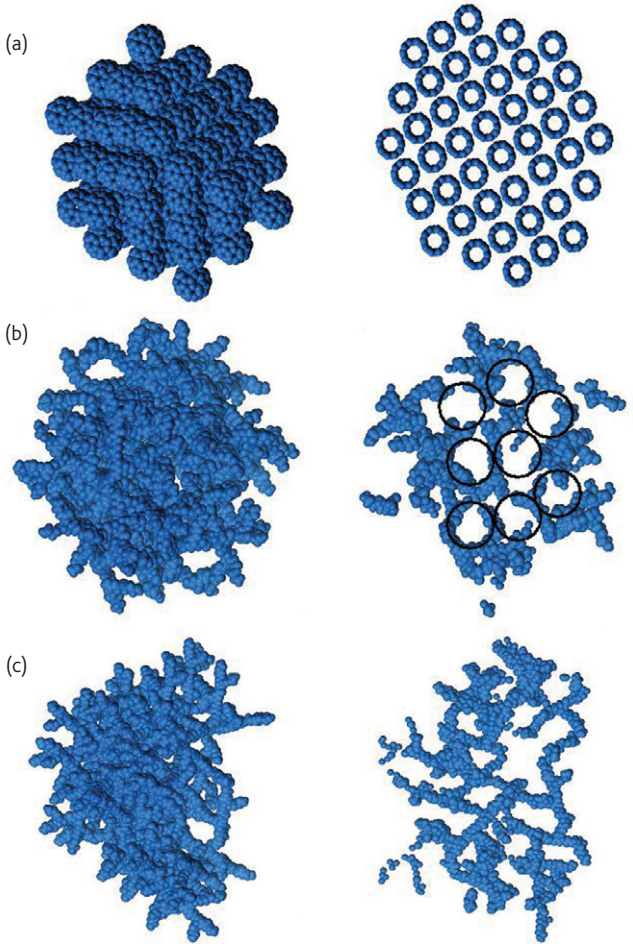

Fig. 12 Three-dimensionals models (on the left) for (a) fullerene C_{60}, (b) dendritic and (c) hyperbranched PAMAM. Slices cut through the central part of the models are shown on the right. PAMAM dendrimers with the structure shown in (b) exhibit relatively open interior with cavities (big open circles) ranging from 5 to 15 Å in diameter.

well ordered and has a very open interior (Fig. 12a, right). A similar approach was adopted to build a model for the hyperbranched PAMAM structure. The only difference was that the degree of branching of the amidoamine building units was kept lower than that with the PAMAM dendrimer. A model atomic configuration that is relaxed and shows a PDF (see Fig. 11c) in good agreement with the experimental data is presented in Fig. 12c. It is worth nothing that both nanostructures shown in Fig. 12b and c are built from the same molecular units and have the same total number of atoms. What is different is the way the individual structural units (polymeric branches) are coupled together and arranged in space[47].

Successful high-energy XRD and atomic PDF studies have also been done on organic/inorganic nanocomposites[48].

Natural 'nanocrystals'

Nature too is a big producer of nanocrystalline materials. A typical example is the microorganism-assisted oxidation of water-soluble

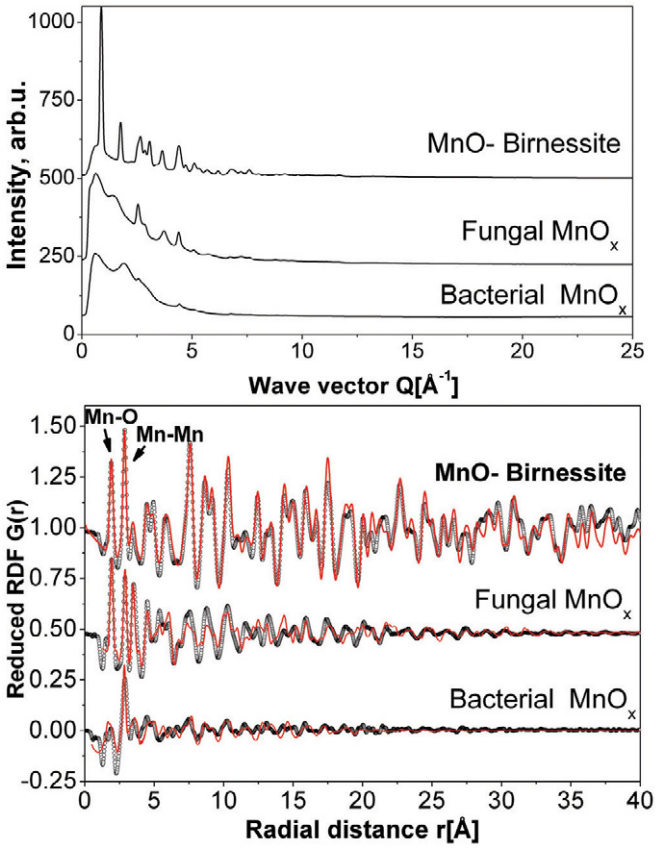

Fig. 13 Experimental XRD patterns (upper part) and the corresponding atomic PDFs for synthetic crystalline, fungal, and bacterial MnO_x. PDF peaks reflecting first neighbor Mn–O and Mn–Mn correlations are marked with arrows. Model PDFs based on the structures shown in Fig. 14a–c are seen to approximate very well the experimental data for birnessite, fungal, and bacterial MnO_x, respectively.

metal ions into insoluble oxides resulting, over time, in the formation of sediments and/or deposits which are a major component of ores and soil. This process turns to be a very efficient way to capture and immobilize pollutant metal ions, and that is why it has been extensively studied recently. To understand a physicochemical process, a very good understanding of the structure of its product is needed. High-energy XRD and atomic PDFs can help here as well. An example is a recent structure study on MnO_x freshly produced by bacteria (*Leptothrix discophora*) and fungi (*Acremonium strictum*)[49]. The experiments were carried out using 115.232 keV X-rays (λ=0.1076 Å) at the 11IDC beamline, APS. Synthetic crystalline MnO_2 (birnessite) was also measured and used as a standard. Experimental XRD patterns and the corresponding atomic PDFs are shown in Fig. 13. Sharp Bragg peaks are present in the XRD pattern for synthetic (polycrystalline) birnessite. The experimental data (only the fit to the PDF data is shown here) can be approximated very well by a model based on a hexagonal type lattice (space group $P6_3/mmc$) with parameters a = 2.84 Å and c = 14.02 Å, with Mn at (0,0,0) and oxygen at (2/3, 1/3, 0.07) positions inside the unit cell. The structure features layers of edge sharing Mn–O_6 octahedra as shown in Fig. 14a. The XRD patterns for both bacterial and fungal MnO_x are very diffuse in nature, a picture typical for nanocrystalline materials. Structural search and refinement guided by the experimental PDF data showed that, at the atomic scale, fungal MnO_x may be described well in terms of a monoclinic lattice (space group $P12/M1$) with parameters a = 9.20(1) Å, b = 2.88(1) Å, c = 9.92(1) Å, α = 90.0°, β = 93.52° and γ = 90.0°. On the other hand, bacterial MnO_x could be described well in terms of a triclinic lattice (space group $P1$) with parameters a = 2.832(5) Å, b = 2.866(5) Å, c = 12.6(5) Å, α = 89.3(2)°, β = 90.5(5)°, and γ = 125.6(5)°. Fragments from these structural models are given in Fig. 14b and c, respectively. The former features a framework of Mn–O_6 units having tunnels that are 3 × 3 octahedra on a side, and the latter comprises a highly defective 'network' of both edge and corner-sharing Mn–O octahedra with a very nonuniform distribution of Mn atoms: the majority (~70%) cluster into 'birnessite-like' layers (dark-shaded in Fig. 14c) and the rest, together with water molecules, fill up the space between those layers (light-shaded octahedra in Fig. 14c). It is amazing to see that microorganisms produce materials that exhibit atomic ordering that is well defined and periodic at the nanoscale, and that nanophase materials produced

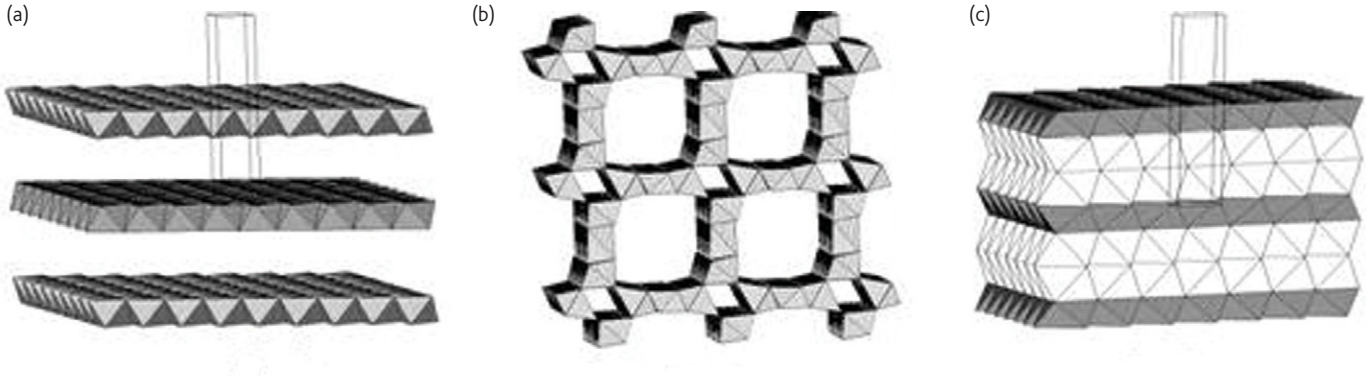

Fig. 14 Fragments from the structures of hexagonal birnessite (a), monoclinic todorokite (b), and a triclinic-type structure featuring birnessite-like 'slabs' of Mn–O_6 octahedra separated by regions of water scarcely populated with Mn ions (light shaded) (c). The unit cell in (a) and (c) is outlined with thin solid lines.

by different microorganisms may have very different atomic-scale structures[49].

High-energy XRD and atomic PDF analysis have also been used to determine the 3-D structure of naturally occurring nanocrystalline materials that have evolved over a very long (geological) period of time such as minerals[50] and clays[51].

Conclusions

High-energy XRD and PDF analysis can yield very good knowledge of the atomic ordering in nanocrystalline materials exhibiting any degree of structural coherence and periodicity. This is important since 'nanocrystalline' materials may appear as quite ordered and periodic atomic arrangements, like ordinary crystals, or as rather disordered and/or nonperiodic atomic arrangements like glasses. In the former case (e.g. V_2O_5 nanotubes), the 3-D structure may be described in terms of a relatively small number of parameters such as the unit cell of the periodic atomic arrangement with its symmetry and the positions and types of the atoms within it. This allows the material's properties to be conveniently computed and predicted. In the second case (e.g. PAMAM dendrimers) the 3-D structure may be described by a sufficiently large (i.e. statistically representative) atomic configuration where the coordinates and chemical type of all atoms are known precisely. Given the recent progress in computer power, this type of structural model should not pose a problem for computing and predicting a nanomaterial's properties.

High-energy XRD and atomic PDF analysis are flexible with respect to a sample's state, morphology, amount, and environment; this approach allows time-dependent studies, and may be done either on laboratory equipment or at the state-of-the-art synchrotron facilities. The combination of high-energy XRD and atomic PDF analysis has the potential to become the standard 'tool' for atomic-scale structure determination in the rapidly developing field of nanoscience and technology. mt

Acknowledgments:

Funding for the work shown here was provide by NSF, DoE, CMU and ARL via several grants. The work presented here reflects the effort of a very large group of scientists. Their names are listed in the papers referred to in this review. Thank you all!

REFERENCES

1. Giacovazzo, C., *et al.*, *Fundamentals of X-ray Crystallography*, Oxford University Press, Oxford, (1998)
2. Klug, H. P., and Alexander, L. E., *X-ray Diffraction Procedures for Polycrystalline and Amorphous Materials*. John Wiley, New York, (1974)
3. Egami, T., and Billinge, S. J. L., *Underneath the Bragg Peaks*, Pergamon Press, Oxford, (2003)
4. Keen, D. A., *J. Appl. Crystallogr.* (2001) **34**, 172
5. Petkov, V., *et al.*, *Phys. Rev. Lett.* (1999) **83**, 4089
6. Toby, B., and Egami, T., *Acta Crystallogr. A* (1992) **48**, 336
7. Toby, B., and Billinge, S. J. L., *Acta Crystallogr. A* (2004) **60**, 315
8. Chupas, P. J., *et al.*, *J. Appl. Crystallogr.* (2007) **40**, 463
9. Qiu, X., et al., *J. Appl. Crystallogr.* (2004) **37**, 110
10. Petkov, V., *et al.*, *Phys. Rev. Lett.* (2000) **85**, 3436
11. Thijsse, B. J., *J. Appl. Crystallogr.* (1984) **17**, 61
12. Rietveld, H. M., *J. Appl. Crystallogr.* (1969) **2**, 65
13. Pradhan, K., *et al.*, *J. Appl. Phys.* (2007) **102**, 044304
14. Petkov, V., *J. Appl. Crystallogr.* (1989) **22**, 387 (available at http://www.phy.cmich.edu/people/petkov/software.html)
15. Qiu, X., *et al.*, *J. Appl. Crystallogr.* (2004) **37**, 678 (available at http://www.pa.msu.edu/cmp/billinge-group/programs/PDFgetX2/)
16. Farrow, C. L., *et al.*, *J. Phys.: Condens. Matter* (2007) **19**, 335219 (available at http://www.diffpy.org/)
17. Proffen, Th., and Neder, R. B., *J. Appl. Crystallogr.* (1997) **30**, 171 (available at http://discus.sourceforge.net/)
18. Neder, R. B., and Proffen, Th., *Diffuse Scattering and Defect Structure Simulations: A Cook Book Using the Program DISCUS*, Oxford University Press, Oxford, (2008)
19. Neder, R. B., *et al.*, *Phys. Status Solidi* (2007) **4**, 3221
20. McGreevy, R. L., and Pusztai, L., *Mol. Simul.* (1988) **1**, 359 (available at http://www.isis.rl.ac.uk/rmc/)
21. Juhas, P., *et al.*, *Nature* (2006) **440**, 655
22. Gateshki, M., *et al.*, *Phys. Rev. B: Condens. Matter* (2005) **71**, 224107
23. Gateshki, M., *et al.*, *J. Appl. Crystallogr.* (2005) **38**, 772
24. Petkov, V., *et al.*, *J. Am. Chem. Soc.* (2000) **122**, 11571
25. Petkov, V., *et al.*, *Phys. Rev. B: Condens. Matter* (2002) **65**, 092105
26. Gateshki, M., *et al.*, *J. Phys. Chem. B* (2004) **108**, 14956
27. Gateshki, M., *et al.*, *Chem. Mater.* (2007) **19**, 2512
28. Pradhan, S. K., *et al.*, *Phys. Rev. B: Condens. Matter* (2007) **76**, 014114
29. Petkov, V., *et al.*, *Phys. Rev. B: Condens. Matter* (2008) **78**, 054107
30. Dmowski, W., *et al.*, *J. Phys. Chem. B* (2002) **106**, 12667
31. Bowman, P. J., *et al.*, *J. Electrochem. Soc.* (2004) **151**, A1989
32. Petkov, V., *et al.*, *J. Phys. Chem. C* (2008) **112**, 8907
33. Bedford, N., *et al.*, *J. Phys. Chem. C* (2007) **111**, 18214
34. Petkov, V., *et al.*, *J. Phys. Chem. C* (2007) **111**, 714
35. Petkov, V., *et al.*, *J. Mater. Chem.* (2005) **15**, 4654
36. Pradhan, S. K., *et al.*, *J. Appl. Phys.* (2007) **102**, 044304
37. Zhang, H., *et al.*, *Nature* (2003) **424**, 1025
38. Neder, R. B., and Korsunskiy, V. I., *J. Phys. Condens. Matter* (2005) **17**, S125
39. Masadeh, A. S., *et al.*, *Phys. Rev. B: Condens. Matter* (2007) **76**, 115413
40. Dmowski, W., *et al.*, *Z. Kristallogr.* (2007) **222**, 617
41. Kistler, M. L., et al., *J. Am. Chem. Soc.* (2007) **129**, 6453
42. Lee, D. C. *et al.*, *Annu. Rep. Prog. Chem. C* (2007) 103, 351
43. Petkov, V., *et al.*, *Phys. Rev. B: Condens. Matter* (2004) **69**, 085410
44. Gateshki, M., *et al.*, *Chem. Mater.* **16** (2004) 5153
45. Gateshki, M., *et al.*, *Z. Kristallogr.* (2007) **222**, 612
46. Paglia, G., *et al.*, *Chem. Mat.* (2006) **18**, 100
47. Petkov, V., *et al.*, *Solid State Commun.* (2005) **134**, 671
48. Petkov, V., et al., *J. Am. Chem. Soc.* (2005) **127**, 8805
49. Petkov, V., *et al.*, *ACSNano* (2008) submitted
50. Michel, F. M., *et al.*, *Science* (2007) **316**, 1726
51. Gualtieri, A. F., *et al.*, *J. Appl. Crystallogr.* (2008) **41**, 402